# Flow dynamics in hyper-saline aquifers:

# hydro-geophysical monitoring and modelling.

Klaus Haaken[1§], Gian Piero Deidda[2], Giorgio Cassiani[3*], Rita Deiana[4], Mario Putti[5], Claudio Paniconi[6], Carlotta Scudeler[5,6], Andreas Kemna[1]

[1] Department of Geophysics, Steinmann Institute, University of Bonn, Meckenheimer Allee 176, 53115 Bonn, Germany

[2] Dipartimento di Ingegneria Civile, Ambientale e Architettura, Università di Cagliari, Via Marengo 2, 09123 Cagliari, Italy

[3] Dipartimento di Geoscienze, Università di Padova, Via Gradenigo 6, 35131 Padova, Italy

[4] Dipartimento di Beni Culturali, Università di Padova, Piazza Capitaniato 7, Palazzo Liviano, 35139 Padova, Italy

[5] Dipartimento di Matematica, Università di Padova, Via Trieste 63, 35121 Padova, Italy

[6] Institut national de la recherche scientifique, Centre Eau Terre Environnement, Université du Québec, Rue de la Couronne 490, G1K 9A9 Québec, Canada

* Corresponding author: giorgio.cassiani@unipd.it

§ currently at Björnsen Consulting Engineers, Maria Trost 3, 56070 Koblenz, Germany

20  **Abstract**

21  Saline-freshwater interaction in porous media is a phenomenon of practical interest

22  particularly for the management of water resources in arid and semi-arid environments,

23  where precious freshwater resources are threatened by seawater intrusion and where storage

24  of freshwater in saline aquifers can be a viable option. Saline-freshwater interactions are

25  controlled by physico-chemical processes that need to be accurately modelled. This in turn

26  requires monitoring of these systems, a non-trivial task for which spatially extensive, high

27  resolution non-invasive techniques can provide key information. In this paper we present the

28  field monitoring and numerical modelling components of an approach aimed at

29  understanding complex saline-freshwater systems. The approach is applied to a freshwater

30  injection experiment carried out in a hyper-saline aquifer near Cagliari (Sardinia, Italy). The

31  experiment was monitored using time-lapse cross-hole electrical resistivity tomography

32  (ERT). To investigate the flow dynamics, coupled numerical flow and transport modeling of

33  the experiment was carried out using an advanced 3D density-driven flow-transport

34  simulator. The simulation results were used to produce synthetic ERT inversion results to be

35  compared against real field ERT results. This exercise demonstrates that the evolution of the

36  freshwater bulb is strongly influencedby the system's (even mild) hydraulic heterogeneities.

37  The example also highlights how the joint use of ERT imaging and gravity dependent flow

38  and transport modelling give fundamental information for this type of studies.

39  **Keywords:** Electrical resistivity tomography; Density-driven flow; Freshwater injection;

40  Hyper-saline; Cross-hole ERT; Flow and transport modeling

## 1. INTRODUCTION

Multiphase flow in porous media has been the subject of intensive study for many decades, motivated, amongst other factors, by important economic considerations linked to the petroleum industry. Another field where interaction of pore fluids having different physical properties is particularly important is saline-freshwater systems. In this case, important density and viscosity differences between saline and fresh waters control the relative motion and mixing of the two phases. Characterizing and modelling these coupled flow and transport phenomena is a very challenging task, particularly in the presence of the hydraulic heterogeneities always present in natural porous media (e.g. Werner et al., 2013; Ketabchi et al., 2016).

The most common situation where saline-freshwater systems have practical environmental and socio-economic implications is related to seawater intrusion in coastal aquifers, often exacerbated by overexploitation of groundwater, particularly in arid and semi-arid regions such as those surrounding the Mediterranean basin (e.g. Kallioras et al., 2010; Rey et al., 2013; Dentoni et al., 2015). Another context where the study of saline-freshwater interactions is highly important is the injection and storage of freshwater in brackish or salty aquifers for later use in agriculture or for domestic purposes, also known as aquifer storage and recovery (ASR;- e.g., Pyne, 1995; Dillon, 2005).

Many studies of density-dependent flow and transport phenomena in porous media have been conducted over the past decades (e.g. Gambolati et al., 1999; Simmons et al., 2001; Diersch and Kolditz, 2002). Instabilities and fingering can take place when denser  water overlies lighter water (e.g., Simmons et al., 2001). Ward et al. (2007) give an introductive literature review on density-dependent modeling, with a particular focus on ASR. The first studies on the injection of freshwater into a saline aquifer were performed by Bear and Jacobs (1965)

66 and Esmail and Kimbler (1967). The latter investigated the tilting of the saltwater-freshwater

67 interface, a phenomenon known as "buoyancy stratification". More recent studies have

68 analyzed the efficiency of ASR for both field and synthetic cases (e.g., Kumar and Kimbler,

69 1970; Moulder, 1970; Kimbler et al., 1975; Ward et al., 2007, 2008; Lu et al., 2011; Zuurbier

70 et al., 2014). Ward et al. (2008) conducted a numerical study to evaluate the efficiency of

71 ASR under density-dependent conditions with anisotropy and heterogeneity of high and low

72 permeable layers. Van Ginkel et al. (2014) studied the possibility to extract saltwater below

73 the freshwater injection to prevent the spreading of freshwater at the top of the aquifer.

74 Alaghmand et al. (2015) investigated fresh river water injection into a saline floodplain

75 aquifer and developed a numerical model  for the optimization of injection scenarios.

76 The behavior of saline-freshwater systems becomes increasingly complex with larger density

77 and viscosity contrasts. To date, very little research has been done on the effects of

78 freshwater injection in highly saline aquifers that can reach total dissolved solids (TDS)

79 concentrations of 100 g/l. Understanding these complex systems is limited not only by the

80 need to develop non-trivial coupled flow and transport models but also by the scarce

81 availability of effective monitoring techniques. The latter are, under field conditions,

82 typically limited to borehole measurements that can only provide point information in

83 spatially heterogeneous hydraulic systems with time-changing salt concentrations.

84 As in many other subsurface characterization problems, a major contribution can be made by

85 non-invasive, spatially extensive, geophysical techniques. In particular, electrical and

86 electromagnetic methods are very suitable in the context of saline-freshwater interactions,

87 since electrical conductivity varies over orders of magnitude depending on solute

88 concentrations. While the use of these methods is common in seawater intrusion studies (e.g.,

89 Goldman and Kafri, 2006; Nguyen et al., 2009)., only few studies have used geophysics to

90 monitor ASR experiments. Davis et al. (2008) used time-lapse microgravity surveys to

monitor the utilization of an abandoned coal mine as an artificial ASR site. Maliva et al. (2009) investigated the use of geophysical borehole logging tools applied to managed aquifer recharge systems, including ASR, to improve the characterization of aquifer properties. Minsley et al. (2011) developed an integrated hydrogeophysical methodology for the siting, operation, and monitoring of ASR systems using electrical resistivity, time-domain electromagnetics, and seismic methods. Parsekian et al. (2014) applied geoelectrical imaging of the subsurface below an aquifer recharge and recovery site alongside with hydrochemical measurements to identify preferential flow paths.

A major step forward in saline-freshwater systems monitoring can be made by improving the efficiency of advanced geophysical techniques, and electrical tomographic methods in particular. Electrical resistivity tomography (ERT) is widely used today in hydrogeological and environmental investigations. Often applied in tracer studies (e.g., Kemna et al., 2002; Vanderborght et al., 2005; Cassiani et al., 2006; Doetsch et al., 2012), ERT is a natural choice for saline-freshwater interaction monitoring, given the correlation between the salinity of a pore fluid and its electrical conductivity. Time-lapse ERT, where only the changes in electrical conductivity over time are imaged (e.g., Kemna et al., 2002; Singha and Gorelick, 2005; Perri et al., 2012), can be especially effective in tracking dynamic processes. Whereas tracer studies are typically designed with injection of a saline tracer into fresh surrounding groundwater, only very few studies have dealt with the inverse case of freshwater injection into a saline formation. For instance, Müller et al. (2010) conducted tracer tests using also a less dense tracer with lower electrical conductivity than the ambient groundwater, monitored with ERT.

The goal of this study is to present a general approach for the characterization, monitoring, and modelling of complex saline-freshwater systems, based on the combination of non-invasive techniques and accurate numerical modelling. To our knowledge, no such a

116 comprehensive hydro-geophysical approach concerning freshwater injection in saline

117 aquifers has been presented so far in the scientific literature, thus we believe this case study

118 can be very useful as a starting point for other, more comprehensive methodical testing.  In

119 this study we limit ourselves to integrating field data and modelling in a loose manner, with

120 no aim at this stage to develop a full data assimilation framework, as implemented elsewhere

121 for simpler systems (e.g., Manoli et al., 2015; Rossi et al., 2015). The key message that can

122 be derived from the joint use of advanced field techniques and advanced numerical modeling

123 is nonetheless apparent in the presented case study, and more complete assimilation

124 approaches are possible provided that the advantages and limitations of the individual

125 components (data and models) are fully understood as shown in the present paper.

126 The approach is presented in the context of a case study where we injected freshwater into a

127 hyper-saline aquifer in the Molentargius Saline Regional Park in southern Sardinia, Italy. The

128 experiment was monitored using cross-hole time-lapse ERT. To investigate the mixing

129 processes, the resulting ERT images are compared with the results of a synthetic numerical

130 study of the same experiment. We consider here both homogeneous and heterogeneous

131 (layered) systems . For a quantitative comparison between the field and synthetic studies,

132 spatial moments of the freshwater bulb are calculated.

133 **2.  FIELD EXPERIMENT**

134 **2.1 Site description**

135 The Molentargius Saline Regional Nature Park is located west of Cagliari in southern

136 Sardinia, Italy (Figure 1). The park is a wetland situated very close to the coastline. The

137 exceptional nature of the site is given by the presence of both freshwater and salty water

138 basins separated by a flat area with mainly dry features (called 'Is Arenas'). The freshwater

139 areas include two ponds that originated as meteoric water retention basins. The salty water

140 areas include the stretches of water of the former system of the Cagliari salt pans.

141 The park area is characterized by an anoligo-miocenic sedimentary succession of some

142 hundreds of meters (Ulzega and Hearty, 1986) overlaid by pleistocenic deposits of marine

143 and continental origin and by alluvial and offshore bar deposits whose origin is still debated

144 (Coltorti et al., 2010; Thiel et al., 2010). This ongoing scientific debate has implications for

145 the comprehension of the phenomenon of hyper-saltiness of the park groundwater.

146 The specific site of investigation is located in the flat dry area within the park (Is Arenas,

147 Figure 1c). The water table of the unconfined aquifer is stable at 5.2 m below ground surface

148 (b.g.s.), and practically neither lateral groundwater flow nor tidal effects are evident. The

149 sediments are composed mostly of sands, with thin layers of silty sand, clayey sand, and silty

150 clay (Figure 2). The groundwater reaches salinity levels as high as three times the NaCl

151 concentration of seawater. Such high salt concentration is likely the long-term legacy of

152 infiltration of hyper-saline solutions from the salt pans dating back, in this area, to Roman

153 times. Electrical conductivity fluid logs (see Figure 3) recorded in boreholes allowed two

154 zones to be discriminated, with a transitional layer in between: (1) from the water table to a

155 depth of 6.5 m the water electrical conductivity is about 2 S/m; (2) below 12 m depth the

156 water electrical conductivity reaches 18.5 S/m. Note that Figure 3 also reports the time-lapse

157 evolution of the vertical electrical resistivity profile as a result of the freshwater injection

158 described in the following section.

159 **2.2 Freshwater injection**

160 Five boreholes for ERT measurements were drilled with 101 mm inner diameter to a depth of

161 20 m and positioned in the shape of a square with 8 m sides (4 corner boreholes) and one

162    borehole at the center (Figure 1b). All boreholes are equipped with a fully screened PVC pipe

163    (screen with 0.8 mm size).

164    In November 2011 19.4 $m^3$ of freshwater with an electrical conductivity of 0.03 S/m, stored

165    in a tank, was injected into the saline aquifer. This was done through the central borehole

166    using a double packer system with an injection segment of 1 m length. The injection chamber

167    was set between 13 m and 14 m b.g.s. The injection rate was entirely controlled by the natural

168    pressure gradient, given by the water head in the tank and the depth of injection (i.e., 13 m to

169    14 m b.g.s. plus 2 m head in the tank above the surface). The natural pressure gradient

170    provided for an initial injection rate of 0.5 l/s. However, during injection (after about 1.5 h)

171    this rate immediately rose to a rate of about 2.75 l/s. We assume that this was due to a

172    clogging of the backfill material which was "de-clogged" after 1.5 h. In total, discharging the

173    tank took about four hours.

174

175    **2.3 ERT monitoring**

176    The direct electrical conductivity measurements described in the previous subsection

177    correspond to the data that would be available as a result of a standard monitoring plan, and is

178    highly insufficient for drawing any conclusions concerning the processes that take place

179    during and after freshwater injection. The available dataset was great enriched by ERT

180    measurements, described below.

181    *Data acquisition*

182    Time-lapse ERT monitoring was applied during the injection experiment in order to image

183    the developing freshwater bulb, "visible" thanks to its lower electrical conductivity compared

184    to the surrounding saltwater. Each borehole bears externally to the casing 24 stainless steel

185    cylindrical electrodes, permanently installed from 0.6 m to 19 m depth with 0.8 m separation,

186    with the exception of the central borehole where the first electrode is placed at the surface

187    and the last at 18.4 m depth. ERT measurements were carried out in a 2D fashion, along two

188    vertical planes diagonal along the boreholes, i.e., one plane was using the borehole numbers

189    1, 5, and 3 and the second plane the borehole numbers 2, 5, and 4 (see Figure 1b), thus

190    making use of 72 electrodes per plane. This choice, in contrast to a full 3D acquisition, was

191    predicated on minimizing the acquisition time, given that the freshwater/saltwater movement

192    was expected to be relatively rapid.

193    The ERT measurements were conducted using a Syscal Pro and adopting different

194    configuration setups, consisting of in-hole dipole-dipole measurements in a skip-zero mode

195    (i.e., adjacent electrodes form a dipole) and cross-hole dipole-dipole (hereafter referred to as

196    bipole-bipole) measurements (Figure 4). Measurements were collected in normal and

197    reciprocal configurations (i.e., exchanging the current and potential dipoles) for estimation of

198    data errors. . The acquisition for one complete measurement frame (consisting of roughy

199    7,300 individual readings) required about 40 minutes.

200    ERT data were acquired in a time-lapse manner to investigate the changes over time caused

201    by the electrical conductivity changes of the developing freshwater bulb within the saline

202    aquifer. The first time step, T0, was acquired before the start of injection in order to compare

203    the following individual time steps with the background image. These were measured on the

204    day of injection, one day after injection, and five days after injection.

205    *Data processing and time-lapse ERT inversion*

206    Due to technical errors (such as bad connection of electrodes, problems with power supply)

207    and varying data quality, the ERT data were processed prior to inversion. In particular, data

208    having a misfit larger than 5% between normal and reciprocal readings were removed.

209 The temperature difference between the groundwater (21 °C) and the injected freshwater

210 (18 °C) was relatively small. Changes in electrical conductivity due to temperature effects are

211 in this case about 5% (see, e.g., Sen and Goode, 1992). Compared to the variation in

212 electrical conductivity between the two fluids, which is about three orders of magnitude, the

213 temperature effect is considered negligible.

214 The ERT field data from the freshwater injection experiment were inverted using the

215 smoothness-constraint inversion code CRTomo. A full description of the code is given by

216 Kemna (2000). In the inversion, the data errors are represented according to a linear model

217 expressed as $\varepsilon = a/R + b$, where $R$ is the measured electrical resistance. For the case at hand

218 the error parameters $a$ (absolute) and $b$ (relative) were set to 0.0001 $\Omega m$ and 10%,

219 respectively.

220 Resistivity images exhibit a variable spatial resolution (e.g., Ramirez et al., 1995; Alumbaugh

221 and Newman, 2000; Nguyen et al., 2009). A useful indicator for this variation is the

222 cumulative sensitivity $\mathbf{s}$ (e.g., Kemna et al., 2002; Nguyen et al., 2009). The sensitivity

223 indicates how a change in electrical resistivity of a certain model cell affects a transfer

224 resistance measurement. Analogously, the cumulative sensitivity quantifies the change of a

225 complete dataset to a changing model cell, and its analysis is an important step in the

226 inversion process. Note that an objective choice for a threshold, that identifies zones where

227 "reliable" vs "unreliable" ERT imaging, is not feasible. In a more qualitative manner one can

228 assume, empirically, that a cumulated sensitivity clearly below 1e-3 leads to weak

229 imaging.Figure 5 shows exemplarily the cumulative sensitivity distribution for the inversion

230 of one dataset (image plane boreholes 1-5-3 at time T0, i.e., the background image). The

231 geometry of the boreholes and the electrodes, in combination with the employed

232  measurement configurations, yields a relatively good coverage within the area of interest (i.e.,

233  mainly the area around the central borehole).

234  In a time-lapse monitoring framework, one is primarily interested in the temporal changes of

235  data and parameters. Therefore, we used the "difference inversion" approach of time-lapse

236  ERT (e.g., LaBrecque and Yang, 2000; Kemna et al., 2002), where the inversion results are

237  changes with respect to the background data at time T0. The advantage of this approach is

238  that modeling errors and data errors correlated over time are cancelled out to a significant

239  degree and associated imaging artifacts that would occur in a standard inversion are

240  suppressed.

241  *ERT imaging results*

242  The ERT dataset was collected under challenging conditions, in particular as the very large

243  salinity contrasts are manifested as extreme electrical conductivity differences over space and

244  time. Large electrical conductivity can occasionally bring DC electrical currents into a

245  nonlinear (non-Ohmic) regime, which in turn can lead to violation of the conditions for the

246  reciprocity theorem (Binley et al., 1995; Cassiani et al., 2006). This has clear implications in

247  terms of data processing, as in particular the error analysis based on reciprocal resistances

248  may not guarantee that direct and reciprocal resistances are equal to each other. Filtering the

249  data according to a reciprocity discrepancy equal to the data error level chosen for the

250  inversion (see above) meant that a fairly large percentage of the data (about 50%) were

251  rejected. Nonetheless a large volume of resistance data was still retained (nearly two

252  thousand  values per time instant).

253  The very high electrical conductivity of the system, which is characteristic of this experiment,

254  has also another consequence: separated inversion of the different electrode configurations

255  (dipole-dipole and bipole-bipole) showed that the bipole-bipole configurations provide better

256 overall results than the dipole-dipole configuration results (not shown here). This is not a

257 common situation, as observed elsewhere in situations of standard resistivity ranges (e.g.,

258 Deiana et al., 2007, 2008), where dipole-dipole data provide higher resolution images than

259 bipole-bipole data that generally only give smoother images as information is averaged over

260 large volumes. In the case shown here, for an in-hole current dipole, the current lines will not

261 penetrate far away from the borehole as they are short-circuited by the large electrical

262 conductivity of saline water surrounding at all times the external boreholes, while for the

263 cross-hole current bipole the current lines "have to" penetrate through the volume between

264 the boreholes. Thus, the sensitivity for the dipole-dipole configurations decreases very

265 strongly with increasing distance from the boreholes. However, the dipole-dipole

266 configuration still manages to provide high sensitivity in the area close to the central

267 borehole, particularly at measurement times where the freshwater bulb surrounds this

268 borehole. Hence, the data coming from both configurations were used for inversion.

269 Figure 6 shows the background image (time T0) before the start of freshwater injection. The

270 electrical resistivity of the saturated zone is very low and vertical changes due to layering of

271 lithologies are not visible. Only a gradual change to higher resistivities in the upper part just

272 below the water table can be seen. This can partly be attributed to the smoothness-constraint

273 applied in ERT inversion. However this feature is also consistent with background

274 conductivity logs (Figure 3).

275 The obtained time-lapse ERT images of the freshwater injection experiment are shown in

276 Figure 7: the distribution of the injected freshwater in the aquifer surrounding the central

277 borehole is clearly visible, in agreement with the time-lapse conductivity logs in Figure 3.

278 The very fast vertical migration of the freshwater plume is also apparent. Between 2 and 6 h

279 after the start of injection, the injection borehole (and its surroundings) is nearly totally filled

280 with freshwater, as confirmed by Figure 3 (after 5 h). However, from the ERT images the

281 freshwater also seems to move downwards below the injection chamber. A few hours after

282 injection, the freshwater plume nearly disappeared in the ERT images, and one day after

283 injection the ERT image seems to have gone back to the background situation (as also

284 confirmed by the conductivity logs in Figure 3).

285 At about 10 m to 11 m depth the difference images show a separation of the plume into two

286 parts. A layer of finer sediments (see Figure 2) is likely to cause this separation. Note that the

287 overall high electrical conductivity masks these lithological differences in the background

288 ERT images. This fine layer is a hydraulic barrier that forces freshwater to flow even more

289 through the preferential flow path provided by the borehole itself and its surrounding gravel

290 pack. Above the fine layer the plume expands again due to the larger hydraulic conductivity

291 of the coarser sediments.

292 During the experiment, the water table as well as the electrical conductivity and the

293 temperature of the borehole fluid were measured manually in all five boreholes. The water

294 table rose about 1.5 m in the injection borehole and about 0.2 m in the surrounding four

295 boreholes. The electrical conductivity log of the central borehole before, during, and after

296 injection is shown in Figure 3. It can be observed that during injection (i.e., about 1 h after

297 start of injection), the saltwater in the borehole was pushed up by freshwater. Shortly after

298 injection stopped (5 h after start of injection) the freshwater filled the entire borehole length,

299 whereas it is visible that the saltwater already entered the borehole in the bottom part (at

300 about 16 m depth) and made its way upwards. One day after the injection experiment, the

301 fluid electrical conductivities  in the central borehole were practically back to their initial

302 values, with small differences between 8 m and 14 m depth still visible. The electrical

303 conductivities of the fluid in the four corner boreholes showed only small changes that

304 nonetheless indicate that part of the freshwater bulb also reached the outer boreholes.

305  **3. SYNTHETIC EXPERIMENT**

306  In order to investigate the behavior of the injected freshwater bulb, and assess in particular

307  the influence of the subsurface hydraulic properties on the bulb evolution, we performed a

308  synthetic study based on the field experiment. This was undertaken using a density-dependent

309  flow and transport simulator. Given the computational burden of the simulations, and our

310  goal of examining in detail some of the governing parameters, we did not use a data

311  assimilation approach at this stage, opting instead for analyses of specific scenarios. We

312  considered four scenarios of hydraulic conductivity distribution, and compared the simulated

313  results to each other and with the field evidence in order to gain some first insights on the

314  dynamic response of the hyper-saline/freshwater system.

315  **3.1 Flow and transport modeling**

316  For the coupled flow and transport modelling of the freshwater injection experiment, we used

317  a 3D density-dependent mixed finite element-finite volume simulator (Mazzia and Putti,

318  2005). This algorithm was shown to be very effective in the presence of advection-dominated

319  processes or instabilities in the flow field induced by density variations (Mazzia and Putti,

320  2006). Here, groundwater flow is described by Darcy's law

$$\boldsymbol{v} = -K_s \boldsymbol{\nabla}(\psi + z), \tag{1}$$

321  where $\boldsymbol{v}$ is the Darcy flux or velocity, $K_s$ is the saturated hydraulic conductivity tensor, $\psi$ is

322  the pressure head and $z$ the elevation head. The hydraulic conductivity is expressed in terms

323  of the intrinsic permeability $k$ and the properties of the fluid as

$$K_s = k \frac{\rho_0 g}{\mu_0}, \tag{2}$$

with $\rho_0$ the density of freshwater, $g$ the gravitational acceleration and $\mu_0$ the viscosity of

freshwater. For density-dependent flow, the density and viscosity of the solution are strongly

dependent on the concentration of the solution:

$$\rho = \rho_0 e^{\epsilon c}, \tag{3.1}$$

$$\mu = \mu_0 e^{\epsilon' c}. \tag{3.2}$$

Here $c$ is the normalized concentration (i.e., the ratio between the concentration of the

solution and the maximum concentration) and $\epsilon$ and $\epsilon'$ are the density and viscosity ratios,

respectively, defined as

$$\epsilon = \frac{\rho_s - \rho_0}{\rho_0}, \tag{4.1}$$

$$\epsilon' = \frac{\mu_s - \mu_0}{\mu_0}, \tag{4.2}$$

where $\rho_s$ and $\mu_s$ are the saltwater maximum density and viscosity, respectively. In our case,

the density and viscosity ratios are $\epsilon = 0.084$ and $\epsilon' = 0.28$, respectively (see also Table 1).

For the exponential laws in Equations 3.1 and 3.2, we used a linear approximation (i.e.,

$\rho = \rho_0(1 + \epsilon c)$, and $\mu = \mu_0(1 + \epsilon' c)$) to reduce the computational cost while introducing

only a negligible inaccuracy.

The mass conservation equations for the coupled flow and transport model can be written as

(Gambolati et al., 1999):

$$S_s(1 + \epsilon c)\frac{\partial \psi}{\partial t} = \nabla \cdot \left[K_s \frac{1 + \epsilon c}{1 + \epsilon' c}(\nabla \psi + (1 + \epsilon c)\boldsymbol{\eta_z})\right] - \phi \epsilon \frac{\partial c}{\partial t} + \frac{\rho}{\rho_0}q^*, \tag{5}$$

$$\boldsymbol{v} = -K_s \frac{1 + \epsilon c}{1 + \epsilon' c}(\nabla \psi + (1 + \epsilon c)\boldsymbol{\eta_z}), \tag{6}$$

$$\phi \frac{\partial c}{\partial t} = \nabla \cdot (D \nabla c) - \nabla \cdot (c\boldsymbol{v}) + qc^* + f, \tag{7}$$

337  where $S_s$ is the specific storage, $t$ is time, $\boldsymbol{\eta_z}$ is the unit vector in z direction, $\phi$ the porosity,

338  $q^*$ is a source (positive)/sink (negative) term, $\boldsymbol{v}$ is the Darcy velocity, *D is hydrodynamic*

339  *dispersion, $c^*$* is the normalized concentration of salt in the injected/extracted fluid, and $f$ is

340  the volumetric rate of injected (positive)/extracted (negative) solute that does not affect the

341  velocity field (Mazzia and Putti, 2006).

342  For the flow and transport model we used a 3D mesh (Figure 8) with about 57,000 tetrahedral

343  elements and 10,000 nodes. The size of the mesh was a good compromise between mesh

344  resolution and computational effort. The computational domain extends for 20 m in the *x* and

345  *y* directions and 15 m in *z* direction, starting at 5 m b.g.s., thus representing only the saturated

346  zone. This choice focuses our attention on the processes of interest and reduces dramatically

347  the numerical complexity of modelling coupled flow and transport processes in variably

348  saturated porous media. However, because a water table rise was observed in the boreholes

349  during the injection experiment, we needed to account for this pressure transient in the flow

350  and transport model. Thus, we simulated a comparable injection experiment using a 3D

351  variably saturated flow simulator (Paniconi and Wood, 1993). The changing pressure values

352  due to the water table rise at 5 m depth were then taken as top boundary conditions for the

353  fully saturated flow and transport model.

354  In addition to the boundary condition described above for pressure and with $c = 0$, we set

355  Dirichlet conditions also on the lateral boundaries with a hydrostatic pressure, according to

356  the concentration dependency $\psi = -(1 + \epsilon c)z$, and Neumann no-flow conditions at the

357  bottom of the mesh. The flow and transport parameter values are given in Table 1. The

358  injection borehole was modeled as a preferential flow path by giving the corresponding cells

359  a large value of hydraulic conductivity. Also the borehole backfill material was included in

360  the simulation by giving it a slightly higher hydraulic conductivity than the surrounding

361 aquifer material. The salt concentration was given as normalized concentration with a value

362 of 1.0 for the saltwater and 0.0 for the injected freshwater. The initial conditions for the

363 concentration in the aquifer were set to honor the transition zone observed in the borehole

364 fluid conductivity log (Figure 2).

365 The conditions for the injection were set by giving the cells that represent the injection

366 chamber (between 13 m and 14 m b.g.s.) a pressure head $\psi$ 2 m higher (from 15 m to 16 m).

367 To simulate the emptying of the tank, the pressure head decreases over time, calibrated after

368 the measured injection rate in the field.

369 The immediate increase of the injection rate, observed in the field experiment, was modeled

370 by a "de-clogging" effect of the material closely surrounding the injection chamber (i.e.,

371 representing the backfill material). This was done by increasing the hydraulic conductivity of

372 the corresponding cells by about one order of magnitude after a corresponding time (i.e.,

373 about 5,000 s). The simulated and true injection rates are compared in Figure 9.

374 Dispersive processes play a minor role for the relatively short time scale of the experiment. In

375 fact, several  dispersivity values were tested and compared (modeling results not shown

376 here); their influence is not significant over the short time scale considered here. Thus, only

377 advective transport is studied.

378 To investigate the influence of heterogeneous hydraulic conductivity distributions in the

379 aquifer, four different scenarios were simulated, including one homogeneous model and three

380 different layered models, with a fine (clay-silt) layer between 10.5 and 11.5 m depth(Table

381 2). The hydraulic conductivity values for the different scenarios were calibrated manually.

382 **3.2 Simulation of ERT monitoring**

383 In order to compare, at least in a semi-quantitative manner, the observed ERT inversions with

384 the results of the synthetic study, it is necessary to convert first the simulated normalized salt

385    concentration from the flow-transport model into bulk electrical conductivity, for example

386    through Archie's (1942) relationship, here expressed for saturated sediments:

$$\sigma_b = \frac{\phi^m}{a} \sigma_w \, , \tag{8}$$

387    where $\sigma_b$ is the bulk electrical conductivity, $a$ is a tortuosity factor, $\sigma_w$ is the electrical

388    conductivity of the fluid, and $m$ is the cementation exponent. The formation factor $F =$

389    $a/\phi^m$ accounts for the pore space geometry. Due to the high salinity of the groundwater in

390    the present case, surface conductivity is assumed to be negligible, and thus Archie's law is

391    safely applicable. Since core data was available from one of the boreholes, it was possible to

392    calibrate Archie's law in the laboratory with $F = 4.6$.

393    The next step is to simulate the field data that would be acquired given the simulated bulk

394    electrical conductivity. For the 3D electrical forward modeling we used the same approach as

395    Manoli et al. (2015) and Rossi et al. (2015). The electric potential field, $\Phi$, for a current

396    injection between electrodes at $r_{S+}$ (current source) and $r_{S-}$ (current sink) is calculated by

397    solving the Poisson equation

$$-\boldsymbol{\nabla} \cdot [\sigma_b \boldsymbol{\nabla} \Phi] = I[\delta(\boldsymbol{r} - \boldsymbol{r}_{S+}) - \delta(\boldsymbol{r} - \boldsymbol{r}_{S-})] \, , \tag{9}$$

398    together with appropriate boundary conditions, where $\sigma_b$ is the given electrical conductivity

399    distribution, $I$ is the injected current strength, and $\delta$ is the Dirac delta function. The mesh for

400    the geoelectrical modeling includes the unsaturated zone, and the top boundary of the mesh

401    (at z = 0 m) was set as a Neumann no-current boundary condition. For the lateral and bottom

402    boundaries we used Dirichlet boundary conditions. Therefore, the mesh size was expanded in

403    all directions with respect to the hydraulic mesh, so that the influence of the fixed voltage

404    boundary conditions on the current lines was negligible.

405    The final step was to process and invert the synthetic ERT data in the same way as the field

406    data.

407    **3.3 Moment analysis**

408    In order to provide a more quantitative comparison between the field and synthetic

409    experiments, we analyzed 2D moments as defined  for example by Singha and Gorelick

410    (2005):

$$M_{ij}(t) = \iint_{\Gamma} C(x,z,t)x^i z^j dx dz \tag{10}$$

411    where $M_{ij}$ is the spatial moment of order $i, j$ between 0 and 2. $x$ and $z$ are the Cartesian

412    coordinates and $dx$ and $dz$ the pixel sizes. $\Gamma$ is the integration domain of interest. The zeroth

413    moment represents the total mass in the system while the vertical first moment, normalized

414    with respect to mass, defines the center of mass in the $z$-direction. The second moments relate

415    to the spread around the center of mass.

416    **4    RESULTS AND DISCUSSION**

417    As a first step, let us consider the results of the synthetic study. Figure 10 shows the salt

418    concentration of the flow and transport simulations for scenario 4, which represents the most

419    complex parameterization of the aquifer and is assumed to be most realistic for the test site

420    (see the site stratigraphy reported in Figure 2). A general upward motion of the injected bulb

421    is visible, with the highest velocities occurring within the injection hole. After some time, the

422    freshwater starts to enter the aquifer along the entire borehole length. Although its density is

423    much less than the density of the surrounding saltwater, the freshwater also moves

424    downwards within the borehole, pushed by the pressure gradients. The 1.2 m thick fine

425    material layer also plays a clear role in the bulb dynamics. This is  expected. In

426 correspondence to this layer the flow only takes place along the borehole and the backfill

427 material. Above the fine layer the plume expands laterally into the aquifer. Also the transition

428 between the saltwater and the upper freshwater layer above 7.4 m depth moves entirely

429 upwards since the overall movement in the model domain is upwards. One can also observe

430 in the simulation results the tilting of the freshwater-saltwater interface in the lower part of

431 the borehole as well as below the groundwater level, as described by Ward et al. (2007,

432 2008). The higher the ratio of hydraulic conductivity between the two layers, the stronger is

433 the tilting, as predicted by Ward et al. (2008) (results not shown here).

434 Figure 11 shows the inverted images for four different subsurface scenarios at time 4.2 h after

435 start of injection for the flow and transport simulations and the synthetic ERT monitoring (see

436 Table 2 for definition of the scenarios). The figure clearly shows the dramatic influence of the

437 hydraulic conductivity distribution on the shape of the freshwater bulb, both in the "real"

438 images and in the corresponding inverted ERT images. Scenario 4, which includes the fine

439 layer, is closest to the field results as already discussed above. However, scenario 3, with just

440 two layers, shows a similar behavior in terms of plume development. In general, given the

441 strong influence that hydraulic conductivity has on the results, it is conceptually possible to

442 try and infer the site's hydraulic properties on the basis of the freshwater injection

443 experiment. However it is also apparent that calibrating *in detail* the true hydraulic

444 conductivity distribution in the field experiment starting from the ERT images alone may be a

445 very challenging task. In fact, while some main features are clearly identifiable, other smaller

446 details may prove difficult to capture.

447 Indeed, the governing hydraulic effect comes from the different conductivities of the upper

448 and lower parts of the aquifer (scenarios 1 + 2 vs. 3 + 4), and the fine layer does not play such

449 an important role as expected a priori. From the simulation results it is difficult to say

450 whether scenario 3 or scenario 4 is closest to reality. However, for scenarios 1 and 2 ERT

451 clearly overestimates the extent of the freshwater plume, whereas for scenarios 3 and 4 the

452 plume extension is reconstructed quite well, in particular in the deeper region (Figure 10).

453 It is instructive to examine in detail (Figure 12) the similarities and differences between the

454 ERT field data and the reconstructed ERT images from the simulation scenario that visually

455 appears better than the others (scenario 4). The simulated ERT images show the same general

456 behavior in response to the injection process and associated plume development as the ERT

457 field results. In the field ERT images the freshwater body disappears much faster. After 24 h,

458 whereas in the field ERT images the freshwater bulb is hardly visible, the simulation still

459 shows its presence. It should be noted that in the simulations the boundary condition at the

460 well is imposed as a Dirichlet (head) condition, so flux is computed depending on the applied

461 head. We applied the head as actually measured in the injection tank. Consequently, the flow

462 is never zero, not even at the end of the experiment. On the other hand, the tilting of the

463 freshwater-saltwater interface as seen in the flow and transport model results is much less

464 visible in the ERT images.

465 The imaged resistivity changes in the field experiment show less contrast than in the synthetic

466 study. The salinity difference between the freshwater and the saltwater is very large and thus

467 so is the NaCl concentration. Within this range, the electrical conductivity of the water might

468 no longer follow a linear relation with concentration (e.g., Wagner et al., 2013), while here it

469 is assumed to be linear. This can lead to a shifting in the contrast when the concentration is

470 converted into electrical conductivity.

471 Note also that the gradual change of electrical conductivity in the transition zone (i.e.,

472 between 5 m and 7.4 m depth) is not visible in the ERT images (Figure 11). In the transport

473 simulations it can be seen that this zone also moves upwards in the aquifer and becomes

474 thinner (Figure 10).

475     Another difference between the field and the synthetic ERT results is the sharpness of the

476     freshwater body: the boundaries appear smoother in the field study. Although dispersion

477     effects were not further investigated in this study, a higher value of $\alpha_L$ and $\alpha_V$ in the

478     simulations would obviously lead to a smoother gradient across the plume boundaries. On the

479     other hand, in the field results this may also be partly explained by the fact that one ERT

480     measurement frame took about 40 minutes; and since the overall plume migration was

481     relatively fast, the process is to some degree smeared in the inverted images.

482     Figure 13 shows the spatial moments ($0^{th}$ moment: total mass; $1^{st}$ moment: center of mass) of

483     the freshwater bulb for the field and synthetic ERT inversion results, as well as the "true"

484     moments from the flow and transport model (see Section 3.3). The total mass is well

485     recovered by the synthetic ERT results (using backwards the same Archie's law

486     parameterization used in the forward modelling). However, the field ERT underestimates the

487     total mass. While this is a known characteristic of moment analysis applied to ERT data for

488     tracer tests (e.g., Singha and Gorelick, 2005), in this specific case it looks likely that the

489     chosen Archie's law parameters are not fully adequate to represent the electrical

490     conductivity-salinity relationship. Considering that even linearity of Ohm's law is

491     questionable at the high salt concentrations observed at the site, one could also question the

492     overall validity of Archie's law. Note that all other factors normally contributing to bad ERT

493     mass recovery under field conditions are the same in the synthetic and the true case, and thus

494     cannot be called into play.

495     In contrast to the total mass, the vertical center of mass is, despite some early oscillations,

496     well recovered also for the field data. This, however, is known to be a very robust indicator

497     (e.g., Binley et al., 2002; Deiana et al., 2007, 2008).

498 Overall, and in spite of the differences described above, the comparison between observed

499 and modelled ERT images is satisfactory, particularly in the face of uncertainties concerning

500 the heterogeneities of the real system that could not be investigated in extreme detail. In

501 addition, we cannot exclude the possibility that the linearity of the current flow equation may

502 be violated in such a highly conductive environment, thus leading to inconsistencies between

503 field reality and theoretical assumptions.

504 Despite the above limitations, the comparison shows that ERT imaging is a viable tool for

505 monitoring freshwater injection in a hyper-saline aquifer. This, by itself, was not an obvious

506 result. The ERT dataset was collected under extreme, challenging conditions. Even so, the

507 ERT data are of fairly good quality considering that we retained only data that passed a fairly

508 strict reciprocity check, knowing that larger reciprocity errors are likely to be related to

509 nonlinear current effects occurring in such high electrical conductivity environments. The

510 study also indicates how an accurate coupled model can mimic in an effective manner the

511 behavior of the observed freshwater bulb that was injected into the domain, and this too was

512 not self-evident.

513 **5  CONCLUSIONS**

514 In this paper we present a hydrogeophysical approach that can be used to study freshwater

515 injections in saline aquifers. In particular the approach is used to monitor and describe a

516 freshwater injection experiment conducted in a hyper-saline aquifer in the Molentargius

517 Saline Regional Park in the south of Sardinia (Italy). The experiment  was monitored using

518 time-lapse ERT in five boreholes. A numerical study of the experiment (density-dependent

519 flow and transport modeling in conjunction with ERT simulations) was carried out to

520 investigate the plume migration dynamics and the influence of different hydraulic

521 conductivity parameterizations. The numerical algorithm of the coupled flow and transport

522 model proved to be stable and accurate despite the challenging conditions.

523 The results demonstrate the feasibility and benefit of using a combination of (a) time-lapse

524 cross-borehole ERT and (b) numerical modelling of coupled flow and transport to predict the

525 same ERT results. The comparison between measured and simulated ERT images was used

526 as the key diagnostics aimed at estimating the system's governing parameters and

527 consequently describing the saltwater-freshwater dynamics. More sophisticated data

528 assimilation techniques can be used to further refine the presented approach in future work.

529 We can conclude from the present study that:

530 (a) the complex dynamics of hyper-saline/freshwater systems can be tracked using high-

531 resolution spatially extensive time-lapse non-invasive monitoring. On the contrary,

532 traditional monitoring techniques alone (e.g., conductivity logs, as in Figure 3) give

533 only a very partial image, largely inconclusive to understand the system dynamics.

534 (b) numerical modelling of these coupled systems is very challenging due to the presence

535 of strong density/viscosity contrasts and large hydraulic conductivity heterogeneities.

536 The latter in particular largely control the dynamics of the saltwater-freshwater

537 interaction. In absence of a robust numerical model it is impossible to estimate the

538 impact of hydraulic heterogeneity on this dynamics.

539 (c) a detailed comparison between field data (here, ERT time-lapse images) and modelled

540 data of the same type enables a better understanding of the behavior of a freshwater

541 bulb injected into a hyper-saline environment.

542 Our study also serves to highlight some of the weaknesses that should be addressed in future

543 work:

544      -      fine-tuning of geophysical constitutive relationships, hydraulic and transport

545             parameters, and system heterogeneities needs to be improved. We managed to bring

546             the match between field and synthetic data to an acceptable level with relatively small

547             effort, but it is very difficult to improve the match further. For instance, in the case

548             presented here the injected freshwater bulb "disappears" from the real ERT images

549             faster than in the simulation results. Also, the mass balance is honored easily in the

550             simulations while in the real data lack of mass is apparent. All of this points towards a

551             number of aspects that could be improved in the data matching. However, the target

552             parameters to be modified for this improvement are not easy to identify, given their

553             very high number and complex nature. Among these, there are hydraulic parameters

554             and dispersivities, and their spatial heterogeneities, and also Archie's law parameters.

555             This task is likely to be challenging even in a rigorous data assimilation framework,

556             and equifinality of model parameterizations is likely.

557      -      the extreme hyper-saline system considered here is likely to exceed the limits of linear

558             relationships between current and voltage (Ohm's law) as well as between electrical

559             conductivity and salinity. Therefore a full nonlinear analysis should be conducted,

560             particularly concerning the electrical behavior of the system. In absence of this, we

561             have to limit ourselves to a semi-quantitative interpretation, as shown here.

562    Finally, with regards to practical aspects of freshwater injection and monitoring in saline

563    aquifers, we can draw the following conclusions:

564      -      although in typical ASR applications the contrasts of density and salinity are usually

565             smaller, this study shows that time-lapse ERT is a powerful monitoring tool for this

566             (and also other) types of hyper-saline applications. ERT can provide spatial

567             information that is unattainable using traditional monitoring techniques (e.g., in

568             boreholes).

569    - the movement and mixing of the freshwater plume can be very fast, thus any ERT

570    monitoring must adopt configurations for quick measurements (e.g., in the conditions

571    represented in this study an acquisition time of less than 30 minutes is recommended).

572    - in hyper-saline systems, measuring reciprocity may not be the ideal error indicator

573    since nonlinear phenomena may be triggered, or, during the time between the normal

574    and reciprocal measurement the system may have already changed, thus invalidating

575    the reciprocity check.

576    The example shown in this paper shows how the joint use of ERT imaging and gravity

577    dependent flow and transport modelling give fundamental information for this type of

578    studies.

579    **Acknowledgements**

580    This research was supported by the Basic Research Project L.R. 7/2007 (CRP2_686, Gian

581    Piero Deidda) funded by the Regione Autonoma della Sardegna (Italy). We thank the Parco

582    Naturale Molentargius-Saline for allowing us to set up a test site in the park. We also thank

583    the field crew from the University of Cagliari (namely Luigi Noli and Mario Sitzia) as well as

584    Marco Mura, Enzo Battaglia, and Francesco Schirru for their work in the field. Special thanks

585    go to Damiano Pasetto and Gabriele Manoli for their support regarding the 3D ERT forward

586    modeling code and Annamaria Mazzia for assistance concerning the numerical experiments.

587    The data can be obtained from the authors upon request.

588

589    **References**

590    Alaghmand, S., Beecham, S., Woods, J. A., Holland, K. L., Jolly, I. D., Hassanli, A., Nouri,

591    H., 2015. Injection of fresh river water into a saline floodplain aquifer as a salt

592        interception measure in a semi-arid environment. Ecol. Eng. 75, 308-322,

593        doi:10.1016/j.ecoleng.2014.11.014.

594    Alumbaugh, D. L., Newman, G. A., 2000. Image appraisal for 2-D and 3-D electromagnetic

595        inversion. Geophys. 65, 1455-1467.

596    Archie, G. E., 1942. The electrical resistivity log as an aid in determining some reservoir

597        characteristics. Trans. of the Am. Inst. of Min., Metall. and Pet. Eng. 146, 54-62.

598    Bear, J., Jacobs, M., 1965. On the movement of water bodies injected into aquifers. J.Hydrol.

599        3, 37-57.

600    Binley, A., Ramirez, A., Daily, W., 1995. Regularised image reconstruction of noisy

601        electrical resistance tomography data. In: Beck, M.S., Hoyle, B.S., Morris, M.A.,

602        Waterfall, R.C., Williams, R.A. (Eds.), Process Tomography — 1995, Proceedings of

603        the 4th Workshop of the European Concerted Action on Process Tomography, Bergen,

604        6–8 April 1995, pp. 401– 410.

605    Binley A.M., G. Cassiani, R. Middleton, and P., Winship, 2002. Vadose zone flow model

606        parameterisation using cross-borehole radar and resistivity imaging, *J. Hydrol.*, 267,

607        147-159.

608    Camporese, M., Cassiani, G., Deiana, R., Salandin, P., 2011. Assessment of local hydraulic

609        properties from electrical resistivity tomography monitoring of a three-dimensional

610        synthetic tracer test experiment. Water Resour. Res. 47, W12508,

611        doi:10.1029/2011WR010528.

612    Camporese, M., Cassiani, G., Deiana, R., Salandin, P., Binley, A., 2015. Coupled and

613        uncoupled hydrogeophysical inversions using ensemble Kalman filter assimilation of

614        ERT-monitored tracer test data. Water Resour. Res. 51(5), 3277-3291,

615        doi:10.1002/2014WR016017.

616  Cassiani, G., Bruno, V., Villa, A., Fusi, N., Binley, A., 2006. A saline tracer test monitored

617        via time-lapse surface electrical resistivity tomography. J. Appl. Geophys. 59, 244-

618        259, doi:10.1016/j.jappgeo.2005.10.007.

619  Coltorti, M., Melis, E., Patta, D., 2010. Geomorphology, stratigraphy and facies analysis of

620        some Late Pleistocene and Holocene key deposits along the coast of Sardinia (Italy).

621        Quat. Int. 222, 19-35, doi:10.1016/j.quaint.2009.10.006.

622  Davis, K., Li, Y., Batzle, M., 2008. Time-lapse gravity monitoring: A systematic 4D

623        approach with application to aquifer storage and recovery. Geophys. 73(6), WA61-

624        WA69, doi:10.1190/1.2987376.

625  Deiana R., G. Cassiani, A. Kemna, A. Villa, V. Bruno and A. Bagliani, 2007. An experiment

626        of non invasive characterization of the vadose zone via water injection and cross-hole

627        time-lapse geophysical monitoring, *Near Surface Geophysics*, 5, 183-194,

628        doi:10.3997/1873-0604.2006030.

629  Deiana R., G. Cassiani, A. Villa, A. Bagliani and V. Bruno, 2008. Model calibration of a

630        water injection test in the vadose zone of the Po River plain using GPR cross-hole

631        data, doi:10.2136/vzj2006.0137 *Vadose Zone J.*, 215-226.

632  Dentoni M., R. Deidda, C. Paniconi, K. Qahman, G. Lecca, 2015, A simulation/optimization

633        study to assess seawater intrusion management strategies for the Gaza Strip coastal

634        aquifer (Palestine), *Hydrogeology Journal*, 23, 249-264; doi: 10.1007/s10040-014-

635        1214-1,

636 Diersch, H.-J. G., Kolditz, O., 2002. Variable-density flow and transport in porous media:
637     approaches and challenges. Adv. Water Resour. 25, 899-944.

638 Dillon, P., 2005. Future management of aquifer recharge. Hydrogeol. J. 13, 313-316,
639     doi:10.1007/s10040-004-0413-6.

640 Doetsch, J., Linde, N., Vogt, T., Binley, A., Green, A. G., 2012. Imaging and quantifying
641     salt-tracer transport in a riparian groundwater system by means of 3D ERT
642     monitoring. Geophys. 77(5), 207-218, doi:10.1190/GEO2012-0046.1.

643 Esmail, O. J., Kimbler, O. K., 1967. Investigation of the technical feasibility of storing fresh
644     water in saline aquifers. Water Resour. Res. 3(3), 683-695.

645 Gambolati, G., Putti, M., Paniconi, C., 1999. Three-dimensional model of coupled density
646     dependent flow and miscible salt transport, in Seawater Intrusion in Coastal Aquifers
647     – Concepts, Methods and Practices, edited by J. Bear, A. H.-D. Cheng, S. Sorek, D.
648     Ouazar, and I. Herrera, pp. 315-362, Kluwer Academic Publishers, Dordrecht, The
649     Netherlands.

650 Goldman, M., Kafri, U., 2006. Hydrogeophysical applications in coastal aquifers, in Applied
651     Hydrogeophysics, edited by H. Vereecken, A. Binley, G. Cassiani, A. Revil and K.
652     Titov, pp.233-254, Springer.

653 Kallioras A., F. Pliakas, I. Diamantis, 2010, Simulation of groundwater flow in a sedimentary
654     aquifer system subjected to overexploitation, *Water Air Soil Pollution*, 211, 177-201,
655     doi: 10.1007/s11270-009-0291-6.

656 Kemna, A., 2000. Tomographic inversion of complex resistivity - Theory and application.
657     Ph.D. thesis, Bochum Ruhr-University, Bochum, Germany.

658   Kemna, A., Vanderborght, J., Kulessa, B., Vereecken, H., 2002. Imaging and characterisation

659       of subsurface solute transport using electrical resistivity tomography (ERT) and

660       equivalent transport models. J. Hydrol. 267, 125-146, doi:10.1016/S0022-

661       1694(02)00145-2.

662   Ketabchi H., D. Mahmoodzadeh, B. Ataie-Ashtiani, C.T. Simmons, 2016, Sea-level rise

663       impacts on seawater intrusion in coastal aquifers: review and integration, *Journal of*

664       *Hydrology*, 535, 235-255, doi: 10.1016/j.jhydrol.2016.01.083.

665   Kimbler, O. K., Kazmann, R. G., Whitehead, W. R., 1975. Cyclic storage of fresh water in

666       saline aquifers. 78pp., Louisiana Water Resour. Res. Inst. Bulletin 10, Baton Rouge,

667       L.A.

668   Kumar, A., Kimbler, O. K., 1970. Effect of dispersion, gravitational segregation, and

669       formation stratification on the recovery of freshwater stored in saline aquifers. Water

670       Resour. Res. 6, 1689-1700, doi:10.1029/WR006i006p01689.

671   LaBrecque, D. J., Yang, X., 2000. Difference inversion of ERT data: a fast inversion method

672       for 3-D in-situ monitoring. Proc. Symp. Appl. Geophys. Eng. Environ. Probl.,

673       Environ. Eng. Geophys. Soc., 723-732.

674   Lu, C., Du, P., Chen, Y., Luo, J., 2011. Recovery efficiency of aquifer storage and recovery

675       (ASR) with mass transfer limitation. Water Resour. Res. 47, W08529,

676       doi:10.1029/2011WR010605.

677   Maliva, R. G., Clayton, E. A., Missimer, T. M., 2009. Application of advanced borehole

678       geophysical logging to managed aquifer recharge investigations. Hydrogeol. J. 17(6),

679       1547-1556, doi:10.1007/s10040-009-0437-z.

680 Manoli, G., Rossi, M., Pasetto, D., Deiana, R., Ferraris, S., Cassiani, G., Putti, M., 2015. An

681     iterative particle filter approach for coupled hydro-geophysical inversion of a

682     controlled infiltration experiment. J. Comput. Phys. 283, 37-51,

683     doi:10.1016/j.jcp.2014.11.035.

684 Mazzia, A., Putti, M., 2005. High order Godunov mixed methods on tetrahedral meshes for

685     density driven flow simulations in porous media. J. Comput. Phys. 208, 154-174,

686     doi:10.1016/j,jcp.2005.01.029.

687 Mazzia, A., Putti, M., 2006. Three-dimensional mixed finite element-finite volume approach

688     for the solution of density-dependent flow in porous media. J. Comput. Appl. Math.

689     185(2), 347-359, doi:10.1016/j.cam.2005.03.015.

690 Minsley, B. J., Ajo-Franklin, J., Mukhopadhyay, A., Morgan, F. D., 2011. Hydrogeophysical

691     methods for analyzing aquifer storage and recovery systems. Ground Water 49(2),

692     250-269, doi:10.1111/j.1745-6584.2010.00676.x.

693 Moulder, E. A., 1970. Freshwater bubbles: A possibility for using saline aquifers to store

694     water. Water Resour. Res. 6, 1528-1531, doi:10.1029/WR006i005p01528.

695 Müller, K., Vanderborght, J., Englert, A., Kemna, A., Huisman, J. A., Rings, J., Vereecken,

696     H., 2010. Imaging and characterization of solute transport during two tracer tests in a

697     shallow aquifer using electrical resistivity tomography and multilevel groundwater

698     samplers. Water Resour. Res. 46, W03502, doi:10.1029/2008WR007595.

699 Nguyen, F., Kemna, A., Antonsson, A., Engesgaard, P., Kuras, O., Ogilvy, R., Gisbert, J.,

700     Jorreto, S., Pulido-Bosch, A., 2009. Characterization of seawater intrusion using 2D

701     electrical imaging. Near Surf. Geophys. 7(5-6), 377-390, doi:10.3997/1873-

702     0604.2009025.

703    Paniconi, C., Wood, E. F., 1993. A detailed model for simulation of catchment scale
704          subsurface hydrologic processes. Water Resour. Res. 29(6), 1601-1620.

705    Parsekian, A. D., Regnery, J., Wing, A. D., Knight, R., Drewes, J. E., 2014. Geophysical and
706          hydrochemical identification of flow paths with implications for water quality at an
707          ARR site. Groundw. Monit. Remediat. 34(3), 105-116, doi:10.1111/gwmr.12071.

708    Perri, M. T., Cassiani, G., Gervasio, I., Deiana, R., Binley, A., 2012. A saline tracer test
709          monitored via both surface and cross-borehole electrical resistivity tomography:
710          Comparison of time-lapse results. J. Appl. Geophys. 79, 6-16,
711          doi:10.1016/j.jappgeo.2011.12.011.

712    Pyne, R. D. G., 1995. Groundwater recharge and wells: A guide to aquifer storage recovery.
713          CRC Press LLC, Boca Raton, Florida.

714    Ramirez, A. L., Daily, W. D., Newmark, R. L., 1995. Electrical resistance tomography for
715          steam injection monitoring and process control. JEEG 1, 39-51.

716    Rey J., J. Martínez, G.G. Barberá, J.L. García-Aróstegui, J. García-Pintado, D. Martínez-
717          Vicente, 2013, Geophysical characterization of the complex dynamics of groundwater
718          and seawater exchange in a highly stressed aquifer system linked to a coastal lagoon
719          (SE Spain), *Environ. Earth Sci.*, 70, 2271-2282, doi: 10.1007/s12665-013-2472-2.

720    Rossi, M., Manoli, G., Pasetto, D., Deiana, R., Ferraris, S., Strobbia, C., Putti, M., Cassiani,
721          G., 2015. Coupled inverse modeling of a controlled irrigation experiment using
722          multiple hydro-geophysical data. Adv. Water Resour. 82, 150-165,
723          doi:10.1016/j.advwatres.2015.03.008.

724    Sen, P. N., Goode, P. A., 1992. Influence of temperature on electrical conductivity on shaly
725          sands. Geophys. 57, 89-96.

726 Simmons, C. T., Fenstemaker, T. R., Sharp Jr., J. M., 2001. Variable-density groundwater

727   flow and solute transport in heterogeneous porous media: approaches, resolutions and

728   future challenges. J. Contam. Hydrol. 52, 245-275.

729 Singha, K., Gorelick, S. M., 2005. Saline tracer visualized with three-dimensional electrical

730   resistivity tomography: Field-scale spatial moment analysis. Water Resour. Res. 41,

731   W05023, doi:10.1029/2004WR003460.

732 Thiel, C., Coltorti, M., Tsukamoto, S., Frechen, M., 2010. Geochronology for some key sites

733   along the coast of Sardinia (Italy). Quat. Int. 222, 36-47,

734   doi:10.1016/j.quaint.2009.12.020.

735 Ulzega, A., Hearty, P. J., 1986. Geomorphology, stratigraphy and geochronology of Late

736   Quaternary marine deposits in Sardinia. Z. Geomorph. N. F. 62, 119-129.

737 Vanderborght, J., Kemna, A., Hardelauf, H., Vereecken, H., 2005. Potential of electrical

738   resistivity tomography to infer aquifer characteristics from tracer studies: A synthetic

739   case study. Water Resour. Res. 41, W06013, doi:10.1029/2004WR003774.

740 Van Ginkel, M., Olsthoorn, T. N., Bakker, M., 2014. A new operational paradigm for small-

741   scale ASR in saline aquifers. Ground Water 52(5), 685-693, doi:10.1111/gwat.12113.

742 Wagner, F. M., Möller, M., Schmidt-Hattenberger, C., Kempka, T., Maurer, H., 2013.

743   Monitoring freshwater salinization in analog transport models by time-lapse electrical

744   resistivity tomography. J. Appl. Geophys. 89, 84-95,

745   doi:10.1016/j.jappgeo.2012.11.013.

746 Ward, J. D., Simmons, C. T., Dillon, P. J., 2007. A theoretical analysis of mixed convection

747   in aquifer storage and recovery: How important are density effects?. J. Hydrol. 343,

748   169-186.

749     Ward, J. D., Simmons, C. T., Dillon, P. J., 2008. Variable-density modelling of multiple-

750                cycle aquifer storage and recovery (ASR): Importance of anisotropy and layered

751                heterogeneity in brackish aquifers. J. Hydrol. 356, 93-105,

752                doi:10.1016/j.jhydrol.2008.04.012.

753     Werner A.D., M. Bakker, V.E.A. Post, A. Vandenbohede, C. Lu, B. Ataie-Ashtiani, C.T.

754                Simmons, D.A. Barry, 2013, Seawater intrusion processes, investigation and

755                management: recent advances and future challenges, *Adv. Water Resources*, 51, 3-26,

756                doi: 10.1016/j.advwatres.2012.03.004.

757     Zuurbier, K. G., Zaadnoordijk, W. J., Stuyfzand, P. J., 2014. How multiple partially

758                penetrating wells improve the freshwater recovery of coastal aquifer storage and

759                recovery (ASR) systems: A field and modeling study. J. Hydrol. 509, 430-441,

760                doi:10.1016/j.jhydrol.2013.11.057.

761

762 **Figures**
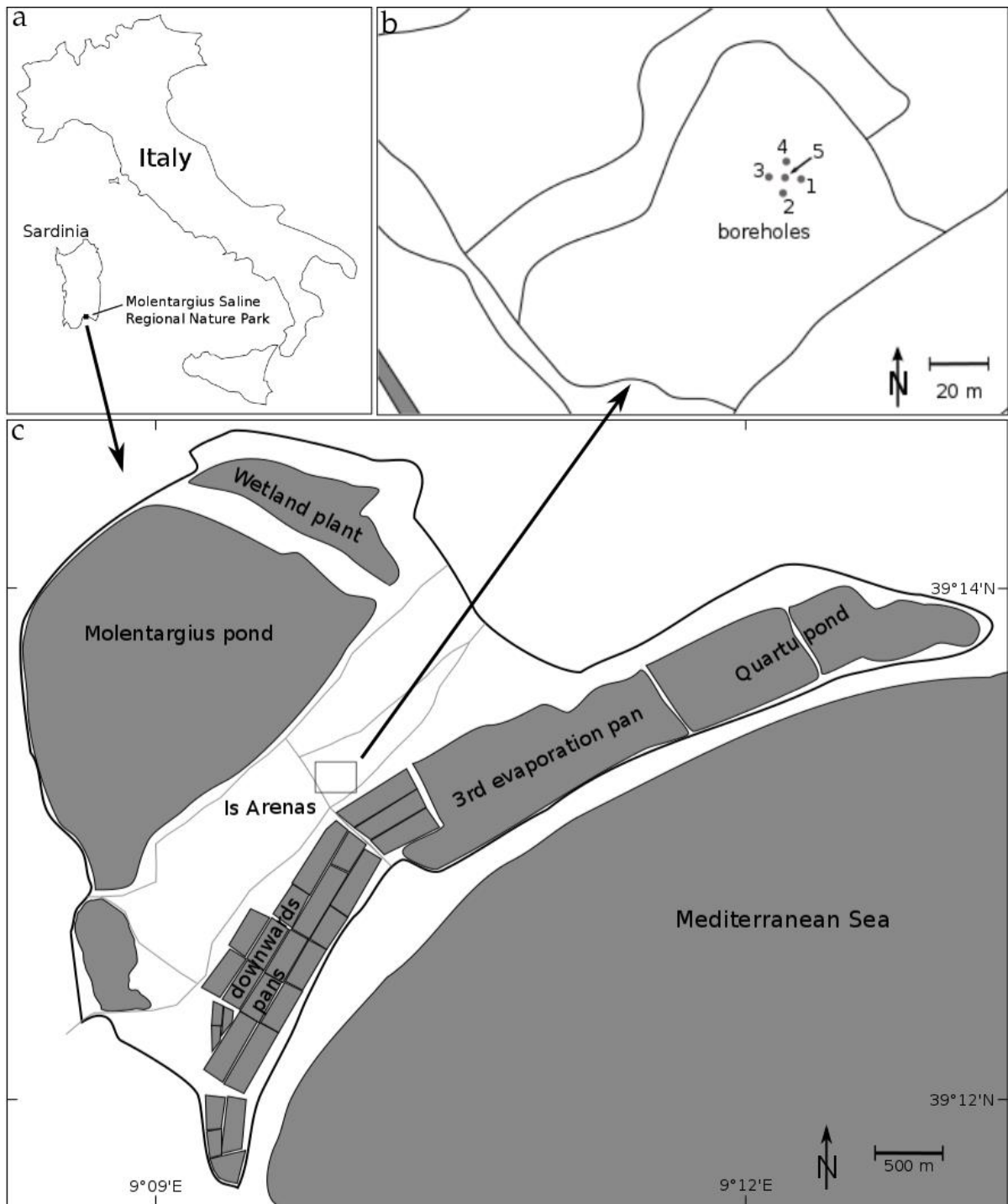
763

764 **Figure 1.** Geographical location of the test site: (a) Molentargius Saline Regional Nature

765 Park located East of Cagliari in southern Sardinia, Italy, (b) Detailed sketch map of location

766 and arrangement of the boreholes, (c) Sketch map of the Molentargius Park (modified after

767 google.earth).

768
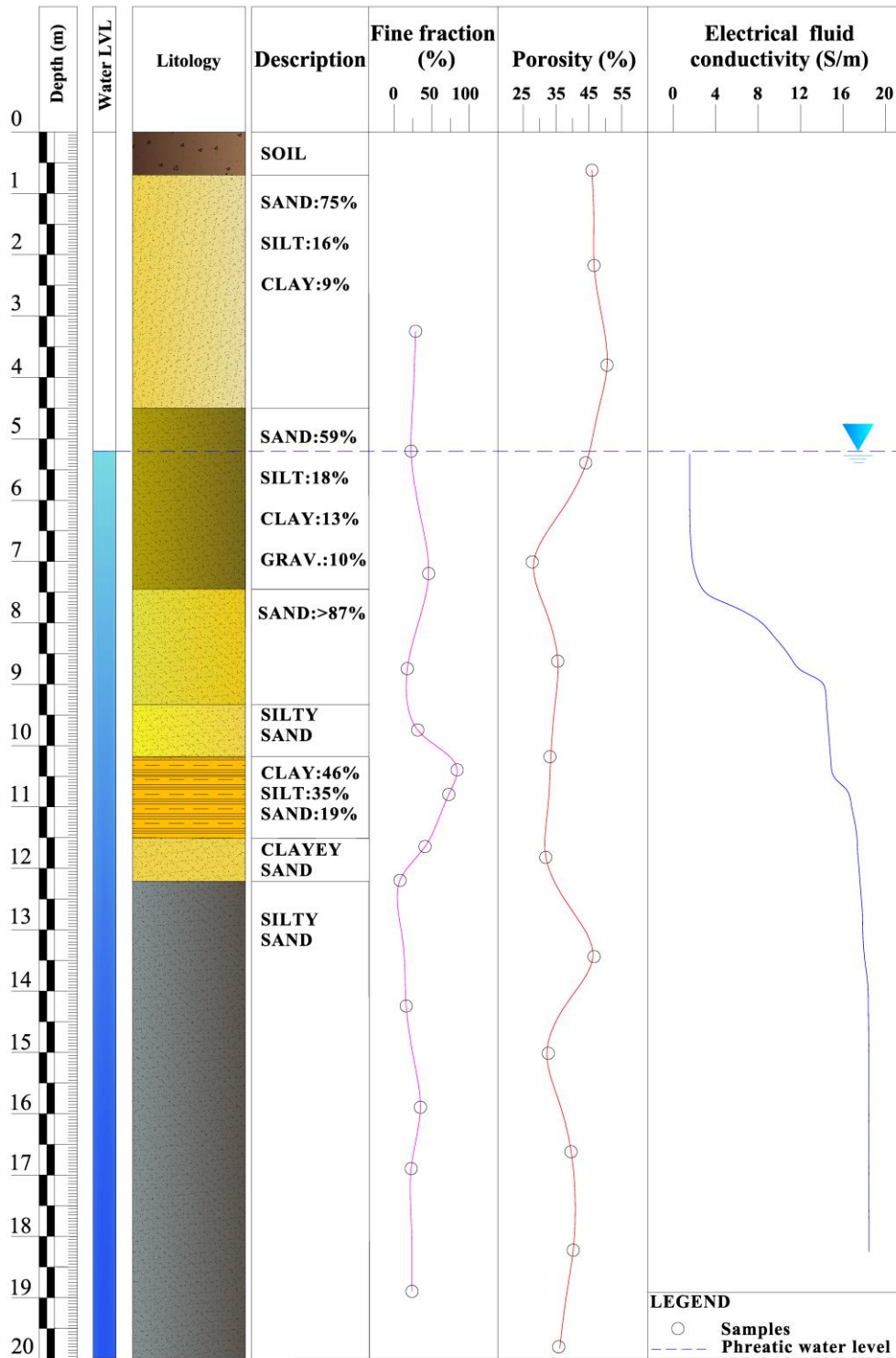
**Figure 2.** Generalized stratigraphy log from the five drilled boreholes including lithology, percentage of fine fraction, and porosity from samples as well as electrical conductivity of borehole fluid. The water table lies at 5.2 m b.g.s..
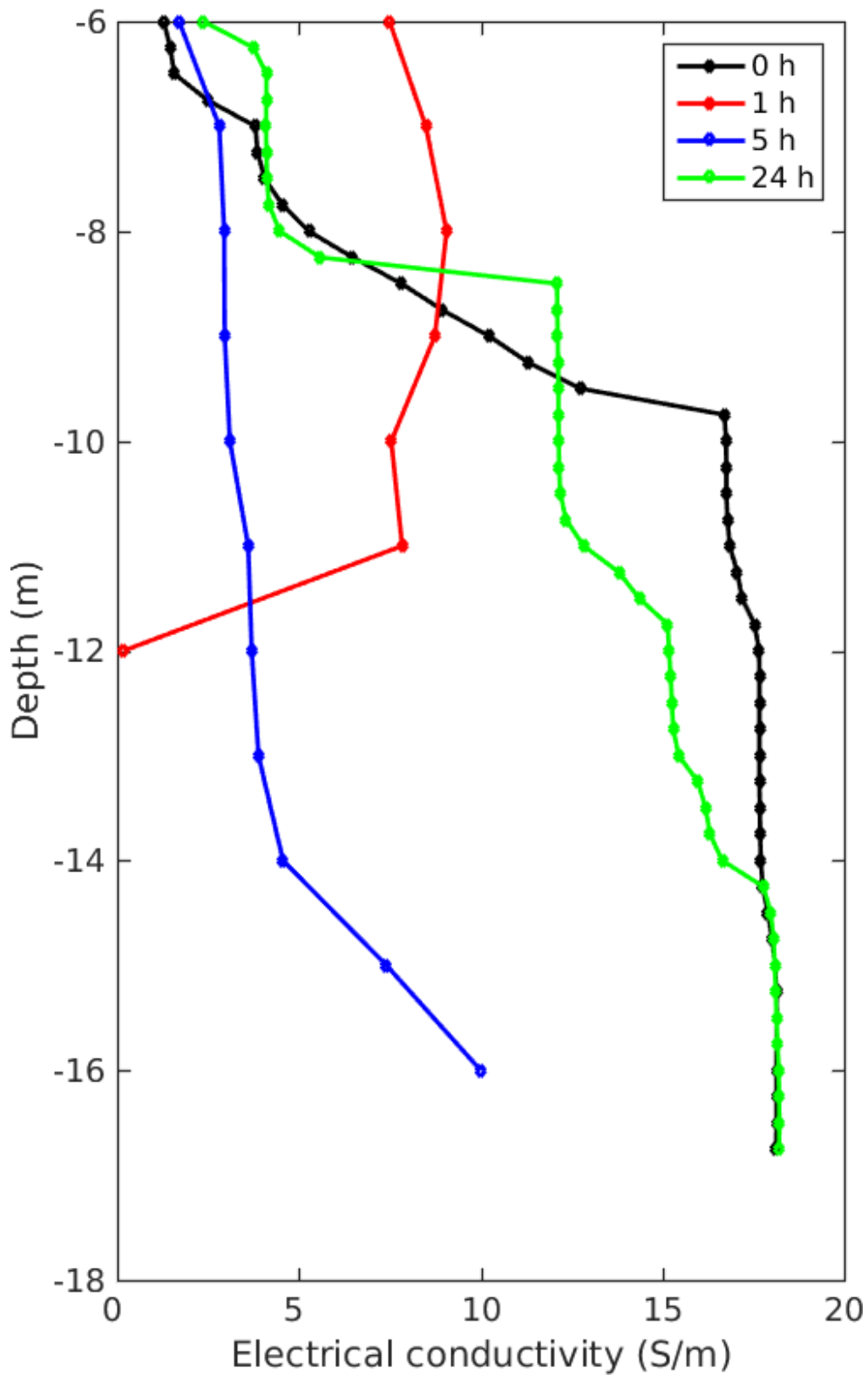
**Figure 3.** Electrical conductivity log of the fluid in borehole 5 at different times after start of freshwater injection (section 2.2). 0 h denotes the background measurement before injection. At 1 h there are no measurements below 12 m b.g.s. because the packer system occupied the borehole.

777
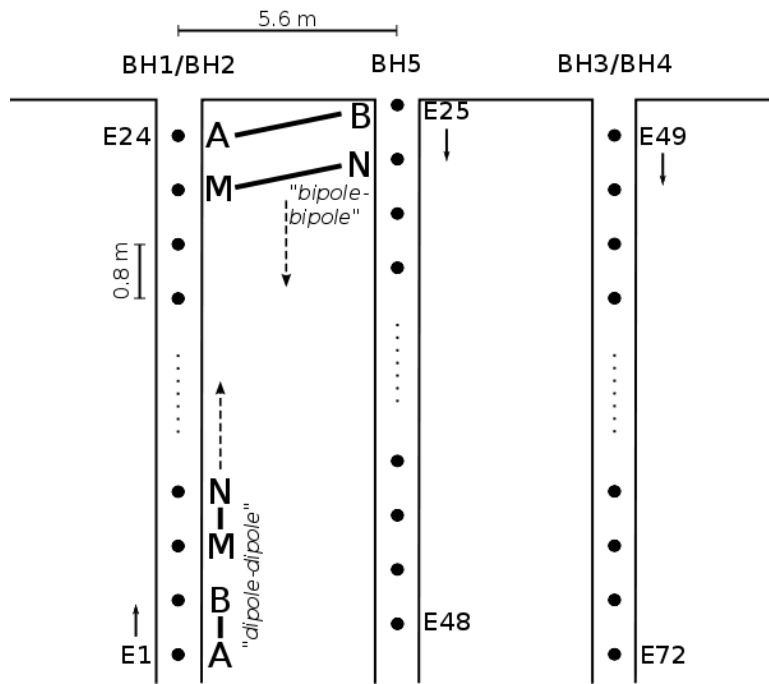
**Figure 4.** Schematic description of the ERT measurement configurations used. For dipole-dipole measurements, one dipole is always within one borehole, the other dipole also moves into the adjacent borehole. Bipole-bipole measurements are done as cross-hole measurements and are also changing as diagonals (i.e., A stays while B moves downwards for up to five electrode positions before A is also moved; similarly for M and N).

783
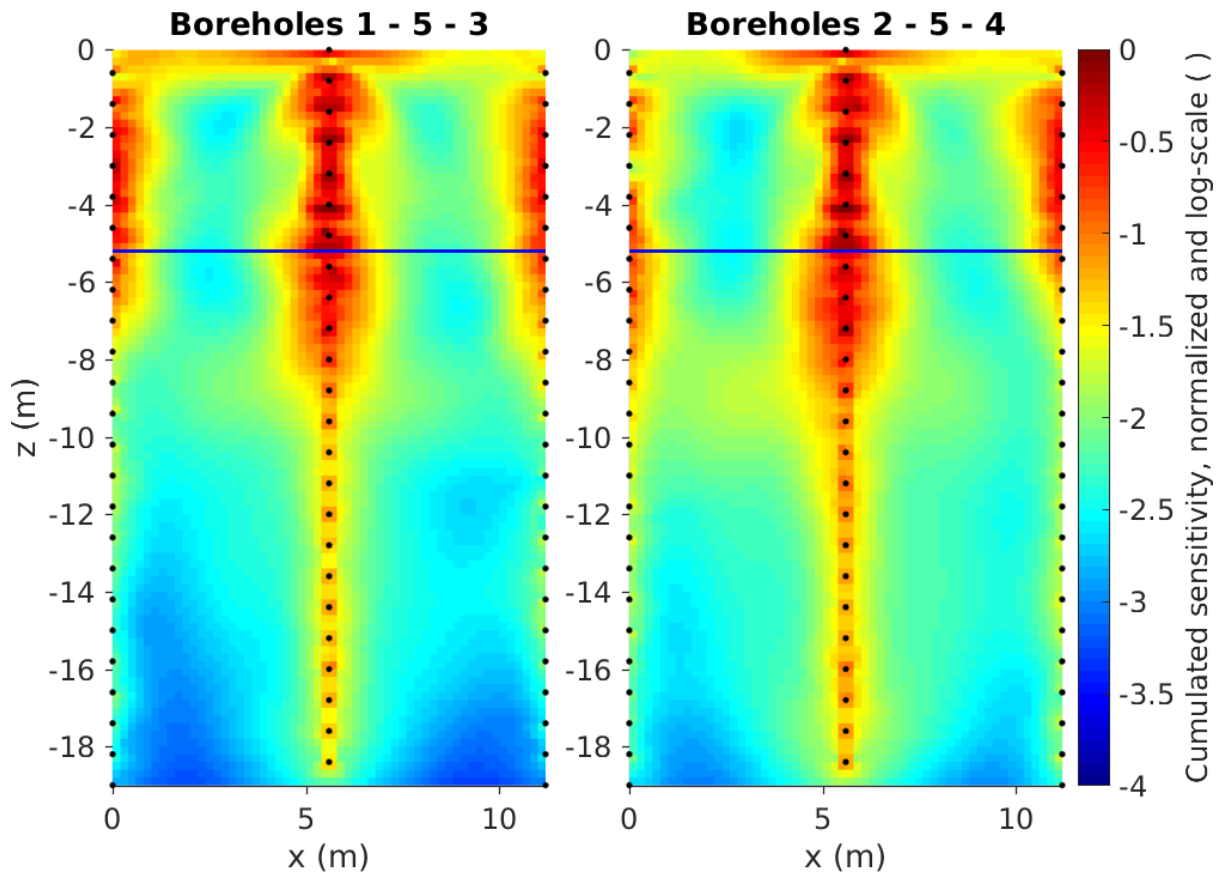
**Figure 5.** Cumulated sensitivity distribution for the inverted background (T0) dataset along

plane $1 - 5 - 3$.
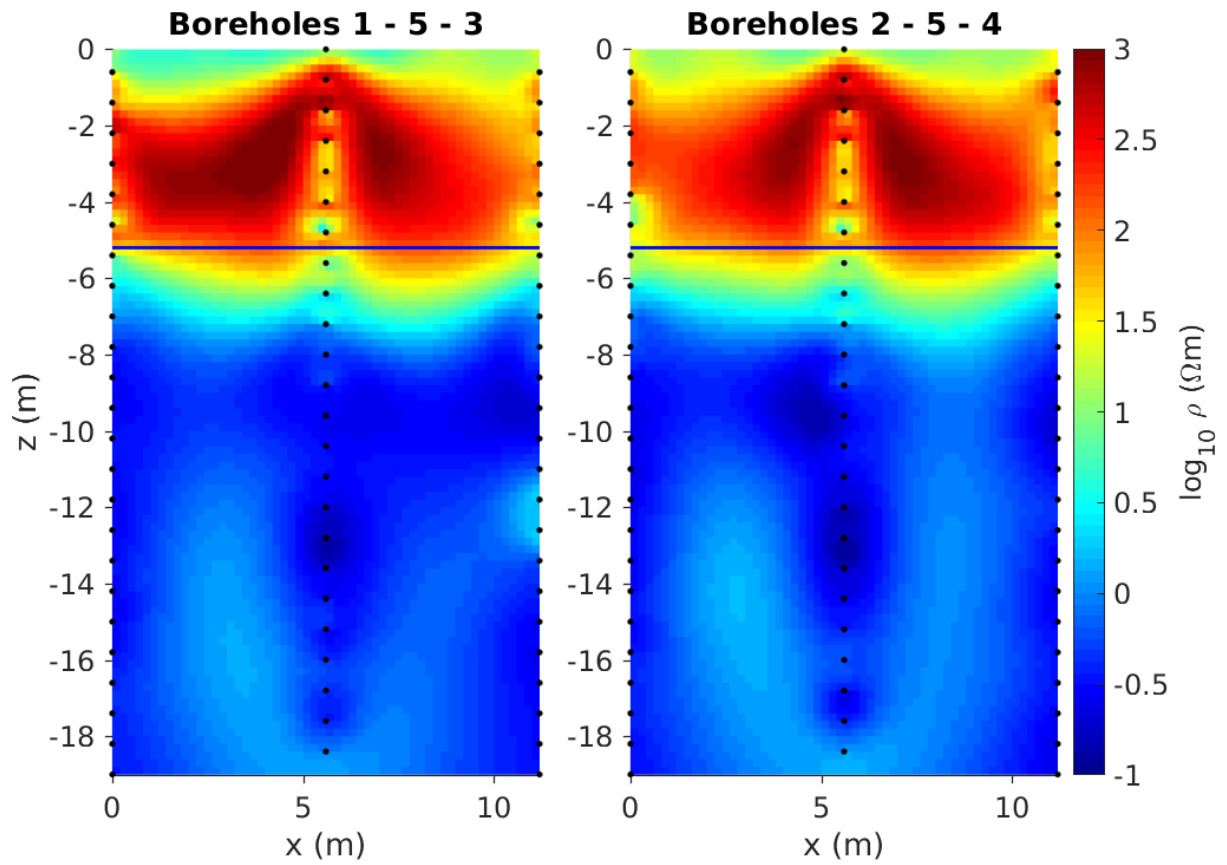
788

789 **Figure 6**: Inverted background (T0) image of plane $2 - 5 - 4$ including the unsaturated zone.

790 Black diamonds denote the position of the electrodes and the blue line shows the groundwater

791 table at 5.2 m b.g.s.

792

793

794
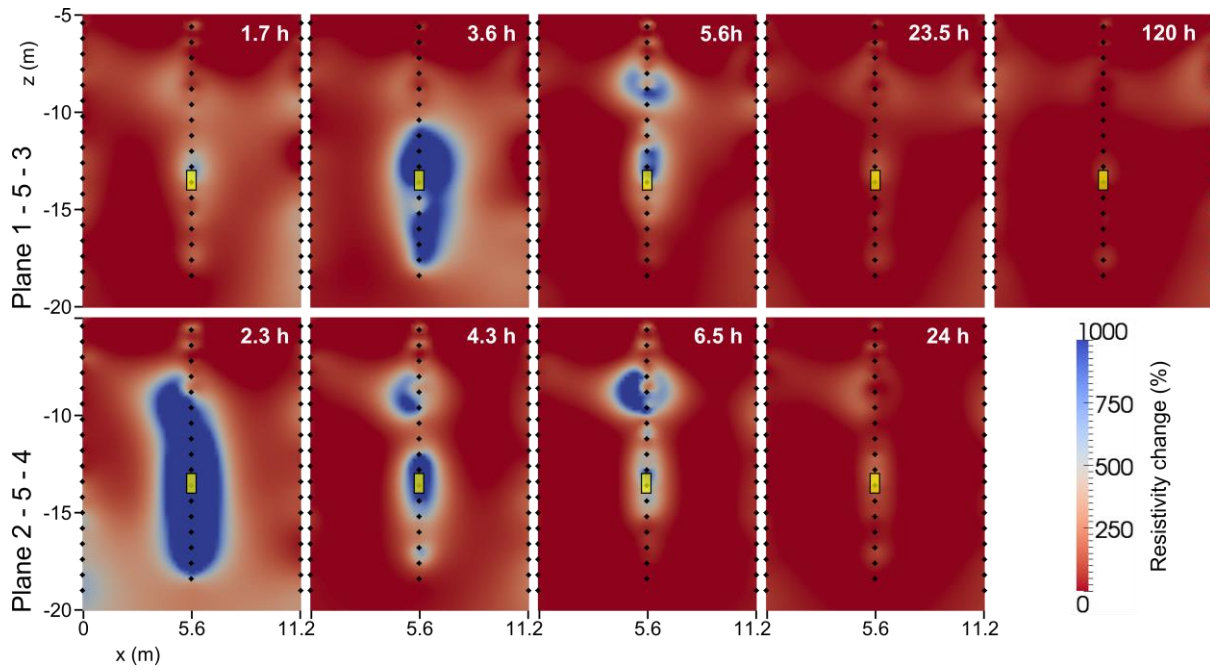
**Figure 7.** Electrical imaging (difference inversion) results for the field experiment at different times (in h after start of injection). The top panel shows the results from borehole plane 1 – 5 – 3 and the bottom panel from plane 2 – 5 – 4. Black diamonds denote the position of electrodes.

799

800
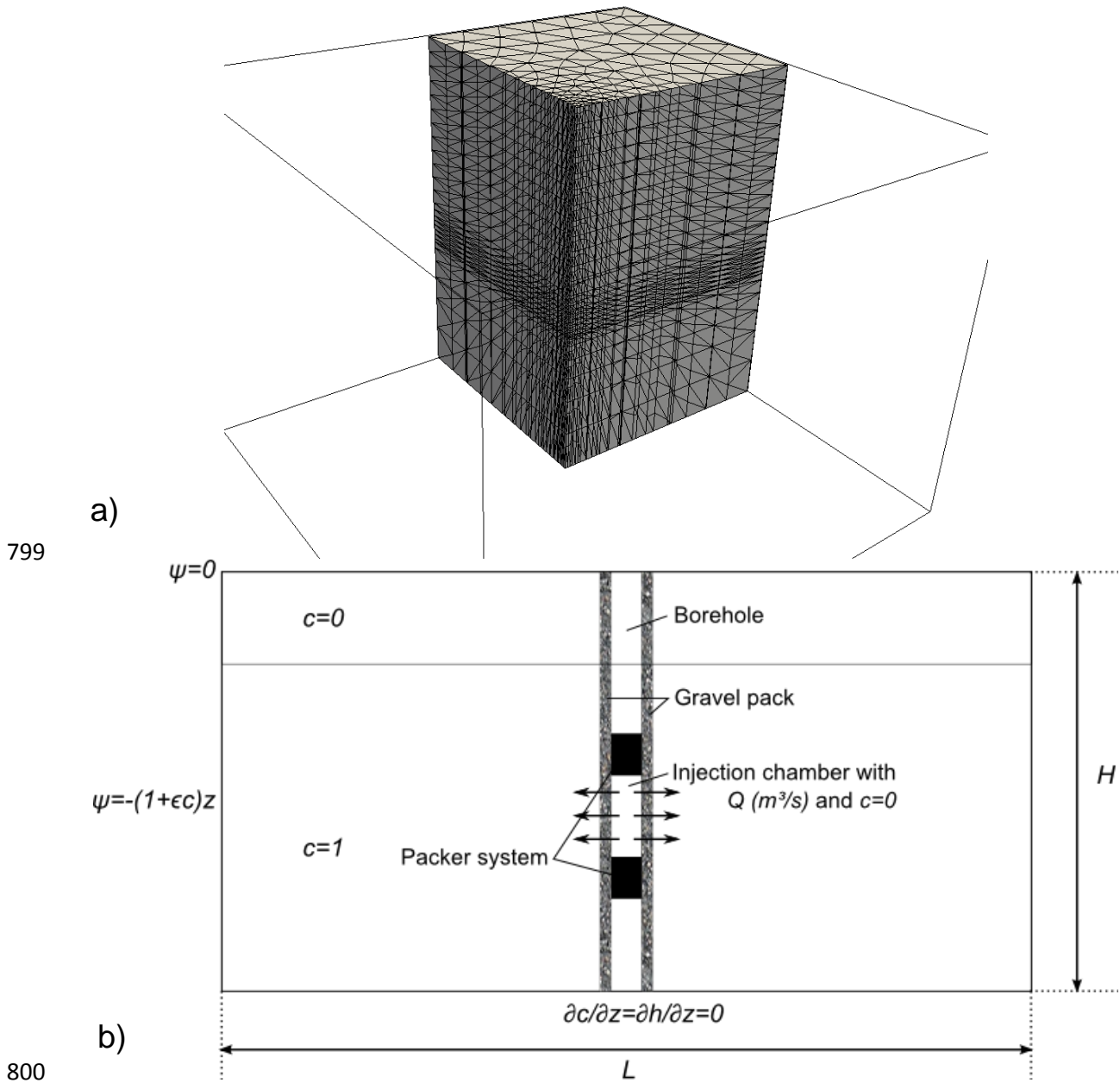
801 **Figure 8.** (a) 3D mesh with refinement in the central part and around injection layers and (b)

802 conceptual model for the synthetic injection experiment.
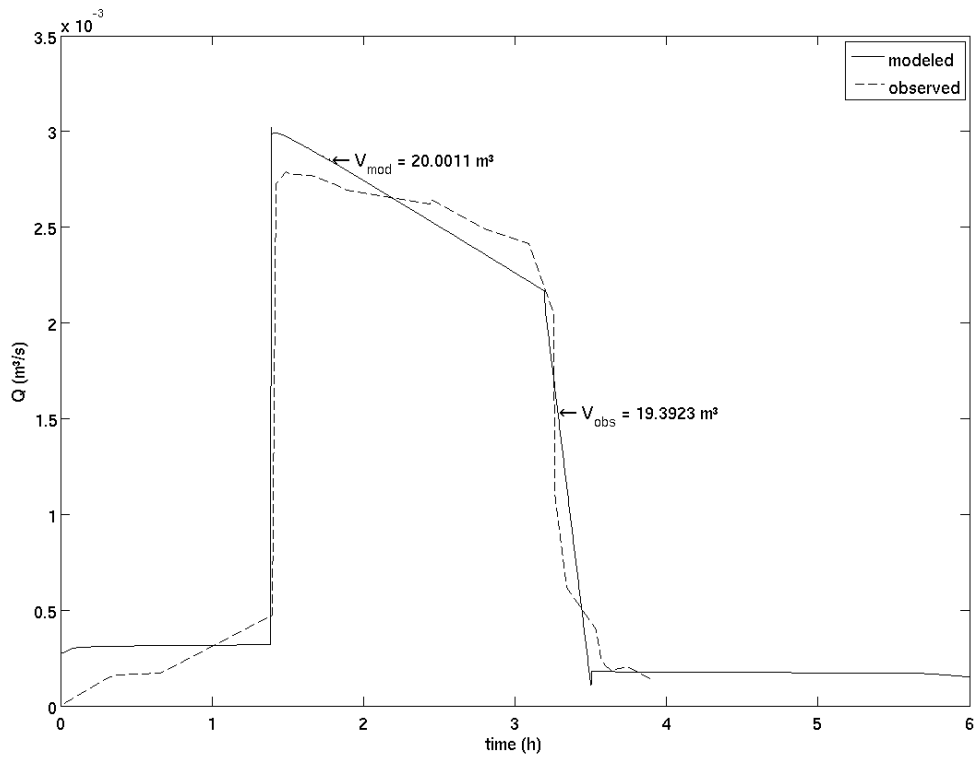
803

804 **Figure 9.** Injection rate of the experiment. The dashed line shows the observed injection in

805 the field experiment (total volume of injected water 19.4 m³) and the solid line shows the

806 calibrated injection rate of the flow and transport model.
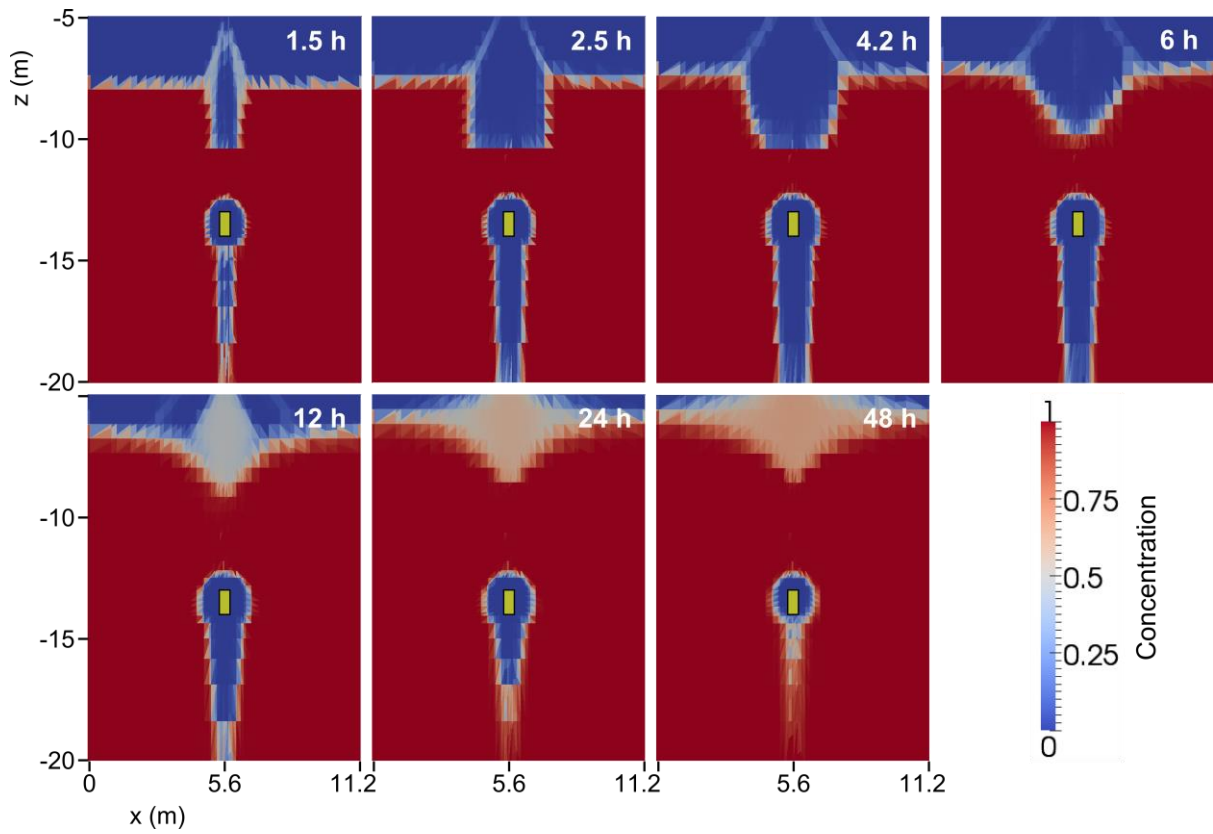
808    **Figure 10.** Flow and transport modeling results at different times (in h after start of injection)

809    for scenario 4 (see Table 2).

810
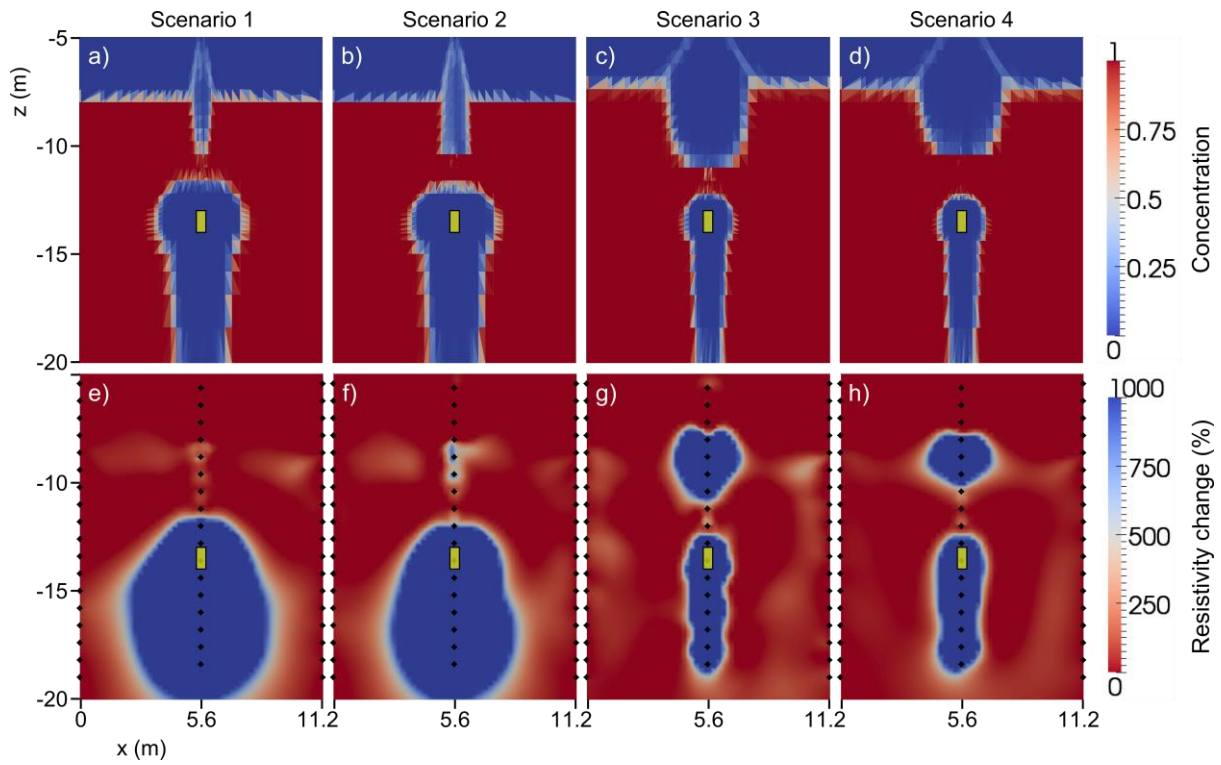
811

812    **Figure 11**: Comparison of simulation results for different hydraulic conductivity

813    parameterizations at time 4.2 h after start of injection. The top panel shows the flow and

814    transport modeling results, the bottom panel the corresponding simulated ERT results. (a) and

815    (e) homogeneous model, (b) and (f) fine layer within homogeneous model, (c) and (g) two-

816    layered system, and (d) and (h) two-layered system including fine layer at interface.

817
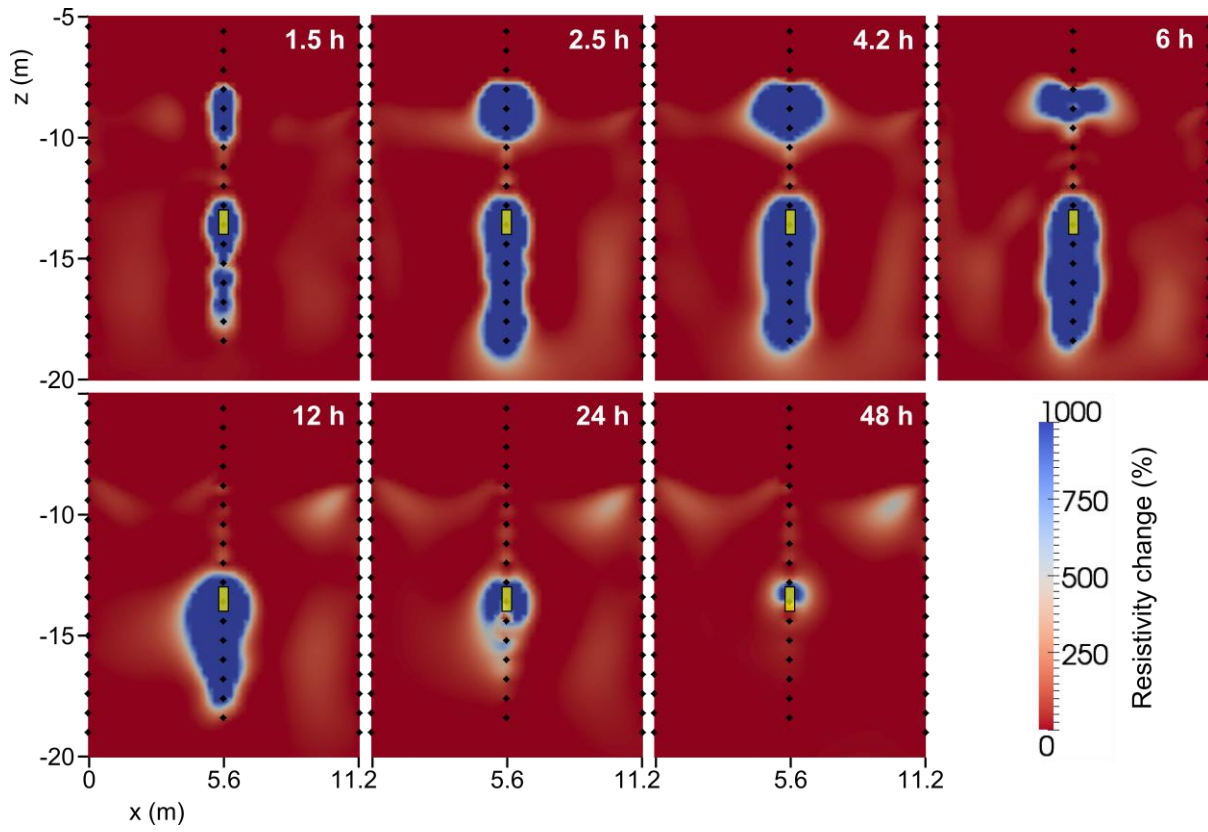
818

819 **Figure** 12: Results of synthetic ERT experiment for selected times (in h after start of

820 injection) for scenario 4 (see Table 2). Black diamonds denote the position of electrodes.

821
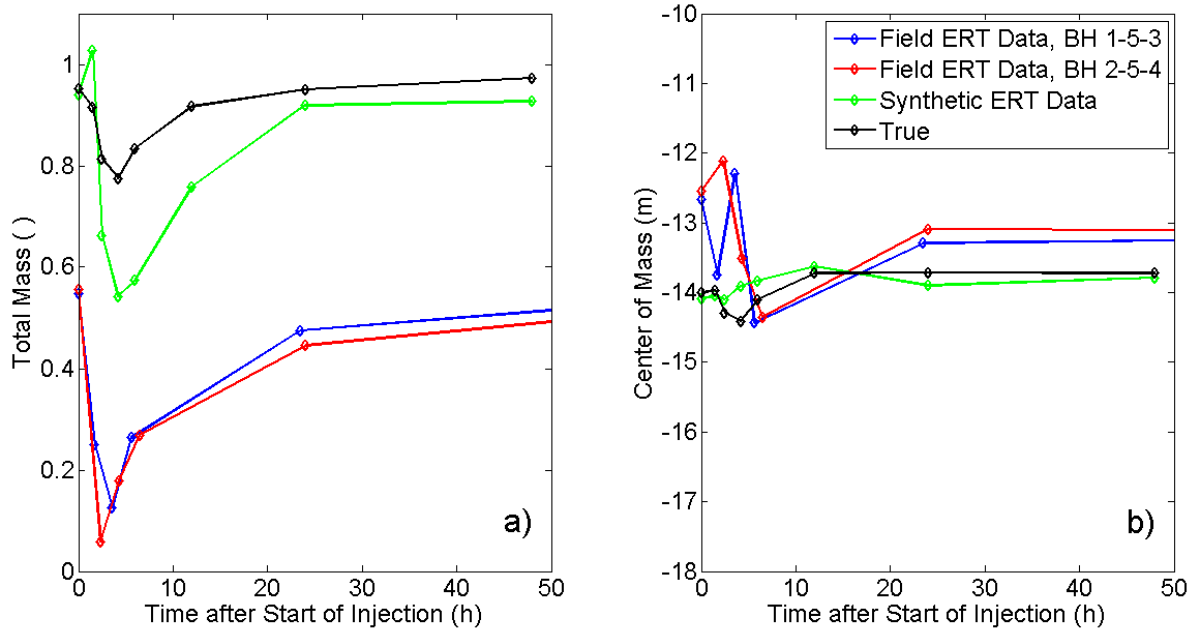
**Figure 13.** Spatial moments for the field ERT data, synthetic ERT data, and the true data from the flow and transport model. The moments for the true field were calculated in 3D while those for the ERT tomograms were calculated in 2D. The field ERT data are separated into the two borehole planes. (a) shows the total mass in the system, normalized, and (b) is the center of mass in the vertical direction.

**Tables**

828   **Table 1.** Flow and transport input parameters for the different zones in the model.

| Parameter | Symbol | Value | Unit |
|---|---|---|---|
| **Model** | | | |
| Aquifer thickness (z direction) | H | 15 | m |
| Horizontal extent (x and y direction) | L | 20 | m |
| | | | |
| **Thickness of aquifer layers** | | | |
| Upper layer | | 5.4 | m |
| Middle layer | | 1.2 | m |
| Bottom layer | | 8.4 | m |
| | | | |
| **Hydraulic conductivities** | | | |
| *Aquifer* | | | |
| Upper layer | | $10^{-5}$-$10^{-3}$ | m s$^{-1}$ |
| Middle layer | | $10^{-6}$-$10^{-5}$ | m s$^{-1}$ |
| Bottom layer | | $10^{-5}$ | m s$^{-1}$ |
| *Well* | | | |
| Injection chamber | | $10^{-3}$ | m s$^{-1}$ |
| Packer system | | $10^{-12}$ | m s$^{-1}$ |
| Remaining well | | 1 | m s$^{-1}$ |
| *Gravel pack* | | | |
| Clogging effect | | $10^{-4}$-$10^{-3}$ | m s$^{-1}$ |
| Remaining gravel | | $10^{-2}$ | m s$^{-1}$ |
| | | | |
| **Solid and fluid properties** | | | |
| Porosity | $\phi$ | 0.35 | - |
| Longitudinal dispersivity | $\alpha_L$ | $10^{-5}$ | m |
| Transverse dispersivity | $\alpha_T$ | $10^{-5}$ | m |
| Diffusion coefficient | $D^*$ | 0 | |
| Density difference ratio | $\epsilon$ | 0.084 | - |
| Viscosity difference ratio | $\epsilon'$ | 0.28 | - |
| | | | |
| **Injection parameters** | | | |
| Injected volume | $V_{mod}$ | 20 | m³ |
| Injection duration | | 3.5 | h |

829

830     **Table 2.** Hydraulic conductivities of each layer for the four different scenarios.

| | Scenario 1 | Scenario 2 | Scenario 3 | Scenario 4 |
|---|---|---|---|---|
| Upper layer | $5 \cdot 10^{-5}$ m s$^{-1}$ | $5 \cdot 10^{-5}$ m s$^{-1}$ | $1 \cdot 10^{-3}$ m s$^{-1}$ | $1 \cdot 10^{-3}$ m s$^{-1}$ |
| Middle layer | $5 \cdot 10^{-5}$ m s$^{-1}$ | $1 \cdot 10^{-6}$ m s$^{-1}$ | | $1 \cdot 10^{-6}$ m s$^{-1}$ |
| Bottom layer | $5 \cdot 10^{-5}$ m s$^{-1}$ | $5 \cdot 10^{-5}$ m s$^{-1}$ | $1 \cdot 10^{-5}$ m s$^{-1}$ | $1 \cdot 10^{-5}$ m s$^{-1}$ |

831